

## What is the Real $K$ Factor?

R. Vogt

Nuclear Science Division, Lawrence Berkeley National Laboratory,  
University of California, Berkeley, California 94720, USA  
and  
Physics Department, University of California, Davis, CA 95616, USA

*Received August 5, 2002*

**Abstract.** The theoretical  $K$  factor, describing the difference between the leading and higher order cross sections, has no precise definition. The definition is sensitive to the order of the fit to the parton densities and the number of loops at which  $\alpha_s$  is evaluated. We describe alternate ways to define the  $K$  factor and show how the definition affects its magnitude and shape for examples of hadroproduction of  $W^+$  bosons, Drell-Yan lepton pairs, and heavy quarks. We discuss which definition is appropriate under certain circumstances.

*Keywords:* gauge bosons, heavy quarks, QCD  
*PACS:* 12.38.Bx

### 1. Introduction

It has been clear for many years that only a leading order, LO, evaluation of quantum chromodynamics, QCD, cross sections is inadequate to describe Drell-Yan, heavy quark, and jet production. For example, at LO lepton pairs from the Drell-Yan process and heavy quark pairs are produced back-to-back with zero transverse momentum,  $p_T$ , of the pair. Thus there is no nonzero Drell-Yan or  $Q\bar{Q}$  pair  $p_T$  at LO. In addition, LO cross sections underestimate the measured total cross sections by up to a factor of two or more.

Next-to-leading order, NLO, evaluations of these cross sections removed many of these inadequacies, especially concerning finite Drell-Yan or  $Q\bar{Q}$  pair  $p_T$  since light quark or gluon emission at NLO keeps the pair from being perfectly back-to-back. In addition, processes such as  $gg \rightarrow gg^* \rightarrow gQ\bar{Q}$  produce high  $p_T$   $Q\bar{Q}$  pairs since the pair takes the entire  $p_T$  of the excited gluon. The magnitude of the Drell-Yan cross section at NLO is in much better agreement with the data. Most modern parton distribution functions, PDFs, are evaluated at NLO and fewer new sets are evaluated at LO. However, only LO matrix

elements are still employed for some processes such as NRQCD quarkonia production, not yet fully calculated at NLO [1]. In addition, the LO matrix elements are inputs to event generators like PYTHIA [2]. Therefore, LO calculations are still of use, either for speed or ease of calculation, if normalized properly relative to NLO.

Proper normalization is important to avoid over- or underestimating the yields with a scaled-up LO calculation. In addition, the shapes of the resulting observable distributions may be different because the LO and NLO PDFs are not identical even though they are fit to the same data. The LO PDFs must be larger than the NLO PDFs in some regions since the NLO total cross sections are generally bigger and the LO PDFs must be larger to compensate. In some cases, certain contributions to NLO evaluations are absent at LO. For example,  $\gamma^*$  and vector boson production, denoted by  $V$ , proceeds only by  $q\bar{q}$  annihilation,  $q\bar{q} \rightarrow V$ , at LO while at NLO,  $q\bar{q} \rightarrow Vg$  and the new process,  $qg \rightarrow Vq$ , with a gluon in the initial state are also possible. Thus, full NLO calculations, using NLO PDFs, two-loop calculations of  $\alpha_s$  and NLO fragmentation functions, where applicable, are preferable.

The ‘so-called’  $K$  factor is used to normalize the LO calculations. The theoretical  $K$  factor is conventionally defined as the ratio between the NLO and LO cross sections. This factor is generally assumed to be constant as a function of the relevant observables. In heavy ion physics, the  $K$  factor has often been assumed to be 2 without justification. To be certain that a LO calculation multiplied by a  $K$  factor does not either over- or underestimate the NLO cross section,  $K$  should be determined according to a clearly defined prescription appropriate to the calculational method.

There is more than one way to define this factor. Before NLO calculations were generally available, the LO calculations were scaled up to the data by an arbitrary factor, the original  $K$  factor. This is an experimental definition,

$$K_{\text{exp}} = \frac{\sigma_{\text{exp}}}{\sigma_{\text{th}}} . \quad (1)$$

If the NLO calculations do not agree with the data, this ratio of data to the higher order calculation can also be defined, usually referred to now as ‘data/theory’, see Ref. [3] for a recent usage. The  $K$  factor is more often determined theoretically. The usual theoretical  $K$  factor is

$$K_{\text{th}}^{(1)} = \frac{\sigma_{\text{NLO}}}{\sigma_{\text{LO}}} \quad (2)$$

where the superscript (1) refers to the fact that only the first order correction is included. When further, higher order, corrections exist, as they do, in part, for Drell-Yan and gauge boson production [4] as well as heavy quark production [5], higher order theoretical  $K$  factors can also be defined, such as

$$K_{\text{th}}^{(2)} = \frac{\sigma_{\text{NNLO}}}{\sigma_{\text{LO}}} , \quad K_{\text{th}}^{(2')} = \frac{\sigma_{\text{NNLO}}}{\sigma_{\text{NLO}}} . \quad (3)$$

We do not go beyond  $K_{\text{th}}^{(1)}$  here.

There is some ambiguity in the definition of  $K_{\text{th}}^{(1)}$ . To demonstrate this, we discuss how the LO and NLO cross sections are calculated. We first define

$$\sigma_{\text{LO}} \equiv \sigma(\alpha_s^n) \quad (4)$$

where the exponent  $n$  is defined as the power of  $\alpha_s$  appropriate for the tree-level partonic process. We do not include the powers of the electroweak coupling constant here for brevity and only concern ourselves with hadroproduction. Thus for Drell-Yan and gauge boson production,  $n = 0$  and  $\sigma_{\text{LO}} \equiv \sigma(1)$ . For direct photon production via  $q\bar{q} \rightarrow \gamma g$  and  $qg \rightarrow \gamma g$ ,  $n = 1$  and  $\sigma_{\text{LO}} \equiv \sigma(\alpha_s)$ . Finally, for heavy quarks produced through the  $q\bar{q} \rightarrow Q\bar{Q}$  and  $gg \rightarrow Q\bar{Q}$  channels,  $n = 2$  and  $\sigma_{\text{LO}} \equiv \sigma(\alpha_s^2)$ . The total NLO cross section is the sum of the LO cross section and the next-order correction,  $\sigma(\alpha_s^{n+1})$ , with one additional power of  $\alpha_s$ ,

$$\sigma_{\text{NLO}} \equiv \sigma_{\text{LO}} + \sigma(\alpha_s^{n+1}) = \sigma(\alpha_s^n) + \sigma(\alpha_s^{n+1}) \quad (5)$$

where we denote the total cross section at NLO as  $\sigma_{\text{NLO}}$ .

The next order correction for Drell-Yan and gauge boson production, along with virtual corrections to  $q\bar{q} \rightarrow V$ , are the new processes  $q\bar{q} \rightarrow Vg$  and  $qg \rightarrow Vq$ . They are first order in  $\alpha_s$ , so that  $\sigma_{\text{NLO}}^{\text{DY}} = \sigma(1) + \sigma(\alpha_s)$ . The NLO correction to heavy quark hadroproduction is  $\sigma(\alpha_s^3)$  so that  $\sigma_{\text{NLO}}^{Q\bar{Q}} = \sigma(\alpha_s^2) + \sigma(\alpha_s^3)$ . The NLO contribution,  $\sigma(\alpha_s^{n+1})$ , is calculated with  $\alpha_s$  evaluated to two loops and with NLO PDFs. However, there is some ambiguity in how to calculate  $\sigma_{\text{LO}}$ . In principle, at each order of  $\alpha_s$ , there should be an appropriate PDF, LO for  $\sigma(\alpha_s^n)$ , NLO for  $\sigma(\alpha_s^{n+1})$ , NNLO for  $\sigma(\alpha_s^{n+2}) \dots$  with  $\alpha_s$  evaluated to one-, two-, and three-loop accuracy respectively. Although possible, at least to NLO, this is usually not done. The NLO PDFs and two-loop  $\alpha_s$  are typically used as defaults for all orders of the cross section. In our calculations, we will compare the magnitude and shape of the cross sections with  $\sigma_{\text{LO}}$  evaluated employing LO PDFs and one-loop  $\alpha_s$ , a full LO cross section, and calculations of  $\sigma_{\text{LO}}$  employing NLO PDFs and two-loop  $\alpha_s$ . We also investigate the effect of these two definitions of  $\sigma_{\text{LO}}$  on the theoretical  $K$  factor for the processes considered.

Thus if  $\sigma_{\text{LO}}$  is fully LO, we define

$$\sigma_{\text{LO}(1)} \equiv \sigma_1(\alpha_s^n), \quad (6)$$

$$\sigma_{\text{NLO}(1)} \equiv \sigma_1(\alpha_s^n) + \sigma(\alpha_s^{n+1}) \quad (7)$$

where the subscript ‘1’ refers to the LO PDFs and one-loop  $\alpha_s$ . If, instead the LO cross section is evaluated with the same PDFs and  $\alpha_s$  as the NLO correction, we have

$$\sigma_{\text{LO}(2)} \equiv \sigma_2(\alpha_s^n), \quad (8)$$

$$\sigma_{\text{NLO}(2)} \equiv \sigma_2(\alpha_s^n) + \sigma(\alpha_s^{n+1}) \quad (9)$$

where now the subscript ‘2’ refers to the NLO PDFs and two-loop  $\alpha_s$ . Recall that the NLO correction,  $\sigma(\alpha_s^{n+1})$ , is always calculated with NLO PDFs and the two-loop evaluation of  $\alpha_s$ .

The total NLO cross section is usually calculated with NLO PDFs and two-loop  $\alpha_s$  at each order, as in Eq. (9), to determine the size of the next-order correction independent of the shape of the PDF and difference in magnitude of  $\alpha_s$ . Thus, the most typical way to evaluate the NLO theoretical  $K$  factor in Eq. (2) is with Eqs. (8) and (9),

$$K_{\text{th},0}^{(1)} \equiv \frac{\sigma_2(\alpha_s^n) + \sigma(\alpha_s^{n+1})}{\sigma_2(\alpha_s^n)} = \frac{\sigma_{\text{NLO}(2)}}{\sigma_{\text{LO}(2)}}. \quad (10)$$

We have labeled this as the 0<sup>th</sup> definition because it is most often used by theorists, see Ref. [4] for an example. It is perhaps more correct to define  $K_{\text{th}}^{(1)}$  based on  $\sigma_{\text{LO}(1)}$ , as in Eqs. (6) and (7),

$$K_{\text{th},1}^{(1)} \equiv \frac{\sigma_1(\alpha_s^n) + \sigma(\alpha_s^{n+1})}{\sigma_1(\alpha_s^n)} = \frac{\sigma_{\text{NLO}(1)}}{\sigma_{\text{LO}(1)}}. \quad (11)$$

Now the subscript ‘1’ on  $K_{\text{th},1}^{(1)}$  refers to the order of the PDFs and  $\alpha_s$  at which  $\sigma_{\text{LO}}$  is evaluated. However, if  $\sigma_{\text{NLO}(2)}$ , is known but the LO calculation,  $\sigma_{\text{LO}(1)}$ , is most convenient, as in an event generator, it might be more advantageous to define the  $K$  factor as

$$K_{\text{th},2}^{(1)} \equiv \frac{\sigma_2(\alpha_s^n) + \sigma(\alpha_s^{n+1})}{\sigma_1(\alpha_s^n)} = \frac{\sigma_{\text{NLO}(2)}}{\sigma_{\text{LO}(1)}}. \quad (12)$$

This last definition maximally mixes the PDF and  $\alpha_s$  evaluations. Thus  $K_{\text{th},2}^{(1)}$  is most dependent on the difference in the shapes of the LO and NLO PDF fits. Note that, in this case only, the  $K$  factor cannot be written as  $K \sim 1 + \mathcal{O}(\alpha_s)$ . The expressions above are written in terms of the total cross sections but are also equally valid for the differential distributions.

We calculate the differential  $K_{\text{th},0}^{(1)}$ ,  $K_{\text{th},1}^{(1)}$ , and  $K_{\text{th},2}^{(1)}$  with  $W^+$ , Drell-Yan and  $Q\bar{Q}$  production as specific examples. In the case of vector bosons,  $K_{\text{th}}^{(1)}$  should most strongly reflect the difference between the LO and NLO PDF evaluations while  $Q\bar{Q}$  production is quite sensitive to the order of the  $\alpha_s$  evaluation. See Ref. [6] for a study of  $K_{\text{th},0}^{(1)}$  in jet production. In our calculations, we use the MRST HO (central gluon) [7] PDFs in the  $\overline{\text{MS}}$  scheme for  $\sigma(\alpha_s^{n+1})$  and  $\sigma_{\text{LO}(2)}$  and the MRST LO (central gluon) [8] PDFs for  $\sigma_{\text{LO}(1)}$  unless otherwise specified.

## 2. $W^+$ Production in $pp$ Interactions

We begin our discussion of the  $K$  factors with the  $W^+$  rapidity distributions. This process is independent of the order of  $\alpha_s$  since at NLO  $\alpha_s$  is always evaluated at two loops. It is also the least differential of all the processes considered. We choose the  $W^+$  of the three gauge bosons because its rapidity distribution is a strong function of the shape of the quark PDFs at LO and NLO. We show our results at the top  $pp$  energy of the LHC, 14 TeV. The dependence of  $K_{\text{th}}^{(1)}$  on rapidity is similar for all gauge bosons so that one case is sufficient for illustration. See Ref. [9] for a comparison of  $K_{\text{th},0}^{(1)}$  for all three gauge bosons. We do not discuss the  $p_T$  dependence of either  $W^+$  or Drell-Yan production because the  $p_T$  of both are zero at LO. Thus  $K_{\text{th}}^{(1)}(p_T)$  cannot be defined for  $W^+$  production, only  $K_{\text{th}}^{(2)}(p_T)$ .

The next-to-leading order, NLO, cross section for production of a vector boson,  $V$ , with mass  $m_V$  at scale  $Q^2$  in a  $pp$  interaction is

$$\frac{d\sigma_{pp}^V}{dy} = H_{ij}^V \int dx_1 dx_2 dx \delta\left(\frac{m_V^2}{S} - xx_1x_2\right) \delta\left(y - \frac{1}{2} \ln\left(\frac{x_1}{x_2}\right)\right) \quad (13)$$

$$\times \left\{ \sum_{q_i, q_j \in Q, \bar{Q}} C^{ii}(q_i, \bar{q}_j) \Delta_{q\bar{q}}(x, Q^2) f_{q_i}^p(x_1, Q^2) f_{\bar{q}_j}^p(x_2, Q^2) \right. \\ \left. + \sum_{q_i, q_k \in Q, \bar{Q}} C^{if}(q_i, q_k) \Delta_{qg}(x, Q^2) \left[ f_{q_i}^p(x_1, Q^2) f_g^p(x_2, Q^2) \right. \right. \\ \left. \left. + f_g^p(x_1, Q^2) f_{q_j}^p(x_2, Q^2) \right] \right\},$$

where  $m_V$  is the boson mass,  $S$  is the center of mass energy squared,  $H_{ij}^V$  is proportional to the LO partonic cross section,  $q_i q_j \rightarrow V$ , and the sum over  $q_i$  runs from  $u$  to  $c$ . At this energy  $Q^2 \gg m_c^2$  so that the  $c$  quark contribution cannot be neglected. The matrices  $C^{ii}$  and  $C^{if}$  contain information on the coupling of the various quark flavors to boson  $V$ . The parton densities in the proton are given by  $f_{q_i}^p(x, Q^2)$  and are evaluated at momentum fraction  $x$  and scale  $Q^2$ . For a vector boson without a fixed mass, as in the Drell-Yan process, the mass distribution can also be calculated by adding a  $dM$  in the denominator of the left-hand side of Eq. (13) and the delta function  $\delta(M - m_V)$  on the right-hand side.

The prefactors  $H_{ij}^V$  are rather simple [4]. In the case of  $W^+$  production,

$$H_{ij}^{W^\pm} = \frac{2\pi}{3} \frac{G_F}{\sqrt{2}} \frac{m_W^2}{S}, \quad (14)$$

where  $G_F = 1.16639 \times 10^{-5} \text{ GeV}^2$  and  $m_W = 80.41 \text{ GeV}$ . For virtual photon production via the Drell-Yan process, there are three contributions to  $H_{ii}^M$ : virtual photon exchange,  $Z^0$  exchange, and  $\gamma^* - Z^0$  interference,

$$\begin{aligned} H_{ii}^M &= H_{ii}^{\gamma^*} + H_{ii}^{\gamma^* - Z^0} + H_{ii}^{Z^0} : \\ H_{ii}^{\gamma^*} &= \frac{4\pi\alpha^2}{9M^2 S} |e_i|^2 \\ H_{ii}^{\gamma^* - Z^0} &= \frac{\alpha}{9} \frac{G_F}{\sqrt{2}} \frac{m_Z^2}{S} \frac{(1 - 4\sin^2 \theta_W)(M^2 - m_Z^2)}{(M^2 - m_Z^2)^2 + m_Z^2 \Gamma_Z^2} |e_i| (1 - 4|e_i| \sin^2 \theta_W) \\ H_{ij}^{Z^0} &= \frac{1}{3} \frac{G_F}{\sqrt{2}} \frac{M^2}{S} \frac{m_Z \Gamma_{Z \rightarrow l^+ l^-}}{(M^2 - m_Z^2)^2 + m_Z^2 \Gamma_Z^2} (1 + (1 - 4|e_i| \sin^2 \theta_W)^2) \end{aligned} \quad (15)$$

where  $\sin^2 \theta_W = 1 - m_W^2/m_Z^2$ ,  $m_Z = 91.187 \text{ GeV}$ ,  $\Gamma_Z = 2.495 \text{ GeV}$ , and  $\Gamma_{Z \rightarrow l^+ l^-} = 3.367\%$ . Note that here we use  $i = j$  since  $i$  and  $j$  must be the same flavor for neutral gauge boson production. Now  $H_{ii}^M$  depends on the pair mass and goes inside the mass integral.

The functions  $\Delta_{ij}(x, Q^2)$  in Eq. (13) are universal for all  $V$  [4]. We work in the  $\overline{\text{MS}}$  scheme. The NLO correction to the  $q\bar{q}$  channel includes the contributions from soft and virtual gluons as well as hard gluons from the process  $q\bar{q} \rightarrow Vg$ . We have, up to NLO [4],

$$\Delta_{q\bar{q}}(x, Q^2) = \Delta_{q\bar{q}}^{\text{LO}}(x, Q^2) + \Delta_{q\bar{q}}^{\text{NLO}}(x, Q^2) \quad (16)$$

$$\Delta_{q\bar{q}}^{\text{LO}}(x, Q^2) = \delta(1 - x) \quad (17)$$

$$\begin{aligned}\Delta_{q\bar{q}}^{\text{NLO}}(x, Q^2) &= \frac{\alpha_s(Q^2)}{3\pi} \left\{ -4(1+x) \ln\left(\frac{Q^2}{m_V^2}\right) - 8(1+x) \ln(1-x) \right. \\ &\quad - 4 \frac{1+x^2}{1-x} \ln x + \delta(1-x) \left[ 6 \ln\left(\frac{Q^2}{m_V^2}\right) + 8\zeta(2) - 16 \right] \\ &\quad \left. + 8 \left[ \frac{1}{1-x} \right]_+ \ln\left(\frac{Q^2}{m_V^2}\right) + 16 \left[ \frac{\ln(1-x)}{1-x} \right]_+ \right\}.\end{aligned}\quad (18)$$

The LO contribution is a delta function. The NLO contribution is proportional to  $\alpha_s$ , calculated to two loops with  $n_f = 5$  active flavors. The first three terms of  $\Delta_{q\bar{q}}^{\text{NLO}}(x, Q^2)$  are the real contributions from  $q\bar{q} \rightarrow Vg$  while the last three terms are the soft and virtual gluon contributions from the  $q\bar{q}$  vertex correction. The general integral of the ‘plus’ functions from soft gluon emission in Eq. (16) is [10]

$$\int_a^1 dx f(x) \left[ \frac{\ln^i(1-x)}{1-x} \right]_+ = \int_a^1 dx \frac{f(x) - f(1)}{1-x} \ln^i(1-x) + \frac{f(1)}{i+1} \ln^{i+1}(1-a). \quad (19)$$

The quark-gluon contribution only appears at NLO through the real correction  $qg \rightarrow qV$ . At this order [4],

$$\begin{aligned}\Delta_{qg}(x, Q^2) &= \Delta_{qg}^{\text{NLO}}(x, Q^2) \\ &= \frac{\alpha_s(Q^2)}{8\pi} \left\{ 2(1+2x^2-2x) \ln\left(\frac{(1-x)^2 Q^2}{xm_V^2}\right) + 1 - 7x^2 + 6x \right\}.\end{aligned}\quad (20)$$

Note that, since at NLO, this contribution is only real, no delta functions or plus distributions appear. Using the delta functions in Eq. (13) we find  $x_{1,2} = \sqrt{Q^2/xS} \exp(\pm y)$  at NLO. For  $\Delta_{q\bar{q}}^{\text{LO}}(x, Q^2)$  and the terms in  $\Delta_{q\bar{q}}^{\text{NLO}}(x, Q^2)$  contributing to the vertex correction in Eq. (18),  $x'_{1,2} = \sqrt{Q^2/S} \exp(\pm y)$ . If we take  $Q^2 = m_V^2$ , all terms proportional to  $\ln(Q^2/m_V^2)$  drop out.

We now define the coupling matrices,  $C^{\text{ii}}$  and  $C^{\text{if}}$ , in Eq. (13). The superscripts represent the initial (i) and final (f) state quarks or antiquarks while the arguments indicate the orientation of the quark line to which the boson is coupled [4]. The  $W^+$  couplings are elements of the CKM matrix. They are nonzero for  $C^{\text{ii}}(q_k, \bar{q}_l)$  if  $e_k + e_l = \pm 1$  and for  $C^{\text{if}}(q_k, q_l)$  if  $e_k = \pm 1 + e_l$ . In both cases, they take the values  $|V_{q_k q_l}|^2$ . Following Ref. [4], we take  $V_{ud} = \cos \theta_C \approx V_{cs}$  and  $V_{us} = \sin \theta_C \approx -V_{cd}$  with  $\sin \theta_C \approx 0.22$ .

The  $W^+$   $q\bar{q}$  convolution in a  $pp$  interaction is

$$\begin{aligned}\sum_{q_i, q_j \in Q, \bar{Q}} f_{q_i}^p(x_1, Q^2) f_{\bar{q}_j}^p(x_2, Q^2) C^{\text{ii}}(q_i, \bar{q}_j) \\ = \cos^2 \theta_C \left( f_u^p(x_1, Q^2) f_d^p(x_2, Q^2) + f_s^p(x_1, Q^2) f_c^p(x_2, Q^2) \right) \\ + \sin^2 \theta_C \left( f_u^p(x_1, Q^2) f_s^p(x_2, Q^2) + f_d^p(x_1, Q^2) f_c^p(x_2, Q^2) \right) + [x_1 \leftrightarrow x_2].\end{aligned}\quad (21)$$

For the  $qg$  channel, we have

$$\sum_{q_i, q_k \in Q, \bar{Q}} \left( f_{q_i}^p(x_1, Q^2) f_g^p(x_2, Q^2) + [x_1 \leftrightarrow x_2] \right) C^{\text{if}}(q_i, q_k) \quad (22)$$

$$= f_g^p(x_2, Q^2) \left( f_u^p(x_1, Q^2) + f_d^p(x_2, Q^2) + f_s^p(x_1, Q^2) + f_c^p(x_1, Q^2) \right) + [x_1 \leftrightarrow x_2] .$$

The couplings do not enter explicitly in the  $qg$  convolution because each distribution is multiplied by  $(\cos^2 \theta_C + \sin^2 \theta_C)$ .

In Fig. 1 we show the  $W^+$  rapidity distributions calculated with Eqs. (6)-(9). The

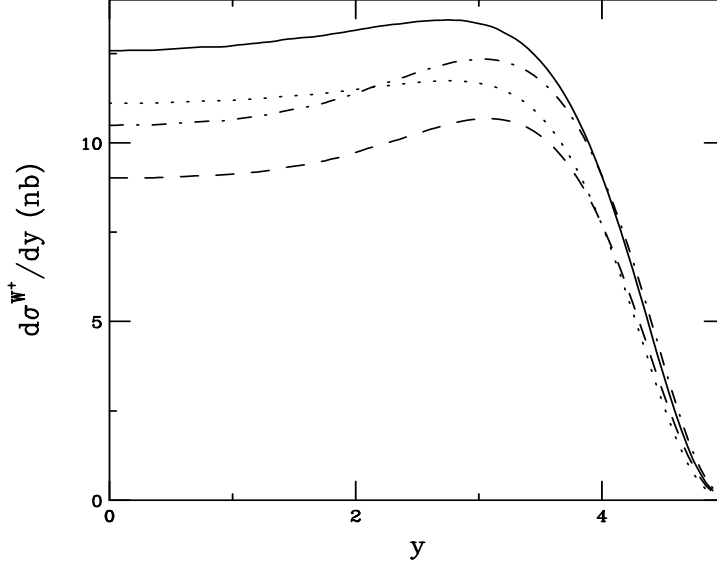


**Fig. 1.** The  $W^+$  rapidity distribution in  $pp$  collisions at 14 TeV evaluated at  $Q = m_{W^+}$ . The solid curve is  $\sigma_{\text{NLO}(2)}$ , the dashed curve is  $\sigma_{\text{LO}(1)}$ , the dot-dashed curve is  $\sigma_{\text{NLO}(1)}$  and the dotted curve is  $\sigma_{\text{LO}(2)}$ .

‘standard’ NLO calculation,  $\sigma_{\text{NLO}(2)}$ , is shown in the solid curve. The accompanying LO result,  $\sigma_{\text{LO}(2)}$ , is given in the dotted curve. The two curves are nearly parallel to each other over most of the available rapidity space. Both increase slowly with rapidity until  $y \sim 3$  where the turnover point is reached. The NLO calculation increases slightly faster than the LO, most likely due to the  $qg$  contribution,  $f_u^p(x_1)f_g^p(x_2)$ , since the gluon distribution increases with decreasing  $x$  when  $x$  is small. The increase with  $y$  is due to the  $f_u^p(x_1)f_d^p(x_2)$  component of the  $q\bar{q}$  annihilation cross section. The valence  $u$  distribution in the proton,  $f_{uV}^p(x_1)$ , is increasing until  $x_1 \sim 0.126$ , corresponding to the peak of  $f_{uV}^p(x_1)$  at  $y \sim 3$ . Likewise  $f_d^p(x_2)$  is rising with decreasing  $x_2$ . Only when  $f_{uV}^p(x_1)$  is falling with growing  $x_1$ , beyond the peak, does the cross section begin to decrease.

The same effect is seen, albeit more strongly, for  $\sigma_{\text{NLO}(1)}$  and  $\sigma_{\text{LO}(1)}$ . We see that  $\sigma_{\text{LO}(2)}$  increases 6% for  $0 < y < 3$  while  $\sigma_{\text{LO}(1)}$  increases by 18% over the same interval. The difference arises primarily because  $f_d^p(x)$  increases faster with decreasing  $x$  at LO than

at NLO. Note also that  $\sigma_{\text{LO}(2)}$  is about 20% larger than  $\sigma_{\text{LO}(1)}$  at  $y = 0$ . This difference is due to the fact that the NLO PDFs are larger in the region around  $x \sim 5.6 \times 10^{-3}$ . As  $y$  increases, the LO valence and sea distributions become closer to the NLO distributions, so that, in the tail,  $\sigma_{\text{LO}(1)} > \sigma_{\text{LO}(2)}$ . This trend is also reflected in the corresponding NLO distributions.

The resulting  $K$  factors are shown in Fig. 2. The ‘standard’  $K$  factor,  $K_{\text{th},0}^{(1)}$ , is the

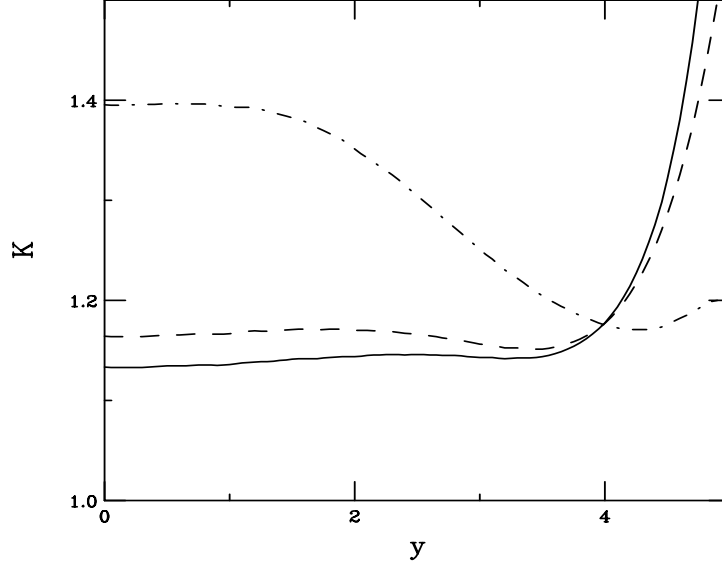


**Fig. 2.** The three  $K$  factors for  $W^+$  production. The solid curve is  $K_{\text{th},0}^{(1)}$ , the dashed is  $K_{\text{th},1}^{(1)}$ , and the dot-dashed is  $K_{\text{th},2}^{(1)}$ .

smallest,  $\sim 1.13$ , for  $0 < y < 3.5$  where it begins to increase. The rise is due to the greater importance of the  $f_q^p(x_1)f_g^p(x_2)$  contribution as  $x_2 \rightarrow 0$ . The factor  $K_{\text{th},1}^{(1)}$  is only slightly higher,  $\sim 1.16$ , and also rather flat over most of the rapidity range. The largest  $K$  factor is  $K_{\text{th},2}^{(1)}$ , as might be expected from inspection of the curves in Fig. 1, due to the greater difference between  $\sigma_{\text{NLO}(2)}$  and  $\sigma_{\text{LO}(1)}$ . The decrease for  $y > 2$  is due to the steeper rise of the LO rapidity distribution as the peak of  $f_{uv}^p(x)$  is approached. The minimum of  $K_{\text{th},2}^{(1)}$  is reached when  $\sigma_{\text{NLO}(2)}$  drops below  $\sigma_{\text{NLO}(1)}$ .

We have also checked the dependence of  $K$  on scale and PDF. The scale dependence enters not only in the PDFs and  $\alpha_s$  but also in the logarithms  $\ln(Q^2/m_V^2)$  in Eqs. (16) and (20). When  $Q^2 = m_V^2$ , as in our calculations so far, the three scale dependent terms in  $\Delta_{q\bar{q}}^{\text{NLO}}(x, Q^2)$  drop out and  $\Delta_{qg}^{\text{NLO}}(x, Q^2)$  only depends on  $\ln((1-x)^2/x)$ . If  $Q^2 > m_V^2$ , the logs are positive, enhancing  $\sigma(\alpha_s)$ , but if  $Q^2 < m_V^2$ , the scale-dependent logs change



sign, decreasing  $\sigma(\alpha_s)$ . Scale evolution increases the low  $x$  density of the sea quarks and gluons while depleting the high  $x$  component and reducing the valence distributions. The  $x$  values do not change when  $Q^2$  is varied. Thus the higher scales also tend to enhance the cross sections. At these large values of  $Q^2$ ,  $\alpha_s$  does not vary strongly so that increasing or decreasing  $Q^2$  by a factor of 16 is not a large effect. The total cross sections are larger when  $Q^2 = 4m_V^2$  and smaller when  $Q^2 = m_V^2/4$ , opposite the scale dependence at lower energies, due to the larger parton densities at low  $x$  and high  $Q^2$ . The same trend was also seen in Ref. [4]. We find that all three definitions of the  $K$  factor exhibit the same  $Q^2$  dependence. Increasing  $Q^2$  gives a 7% larger  $K$  factor while decreasing  $Q^2$  reduces the  $K$  factors by  $\sim 10\%$  for the MRST set.

The variation of the results with PDF is also significant. The MRST and CTEQ [11] results are similar but the CTEQ cross sections are a few percent higher. In this case, the  $\sigma_{\text{LO}(2)}$  and  $\sigma_{\text{NLO}(2)}$  distributions are not as broad as  $\sigma_{\text{LO}(1)}$  and  $\sigma_{\text{NLO}(1)}$ . The peak of  $\sigma_{\text{LO}(2)}$  is at  $y < 3$  while  $\sigma_{\text{LO}(1)}$  peaks at  $y \sim 3.2$ . Because of this difference,  $K_{\text{th},2}^{(1)}$  is not independent of rapidity anywhere but decreases almost to unity where  $\sigma_{\text{LO}(1)} \sim \sigma_{\text{NLO}(2)}$ . When the GRV 98 distributions [12] are used, the rise with rapidity is much stronger than that in Fig. 1. However, now the differences between  $\sigma_{\text{LO}(1)}$  and  $\sigma_{\text{LO}(2)}$  are rather small,  $\sigma_{\text{LO}(1)}$  peaks about 0.25 units of rapidity higher than  $\sigma_{\text{LO}(2)}$  and with a slightly larger value. In this case, the  $K$  factors are all smaller than for MRST,  $K_{\text{th},0}^{(1)} \sim K_{\text{th},1}^{(1)} \sim 1.09$ . Now even  $K_{\text{th},2}^{(1)}$  is only a few percent different than the other two definitions over two units of rapidity.

### 3. Drell-Yan Production in Pb+Pb Interactions

We now discuss dilepton production in the Drell-Yan process where  $\alpha_s$  also does not enter until NLO, as in the previous section, but the LO cross sections are more differential, depending on pair mass,  $M$ , and rapidity. Since, at collider energies, the Drell-Yan contribution to the dilepton continuum is small compared to heavy quark decays and will probably not be cleanly separated, we discuss the Drell-Yan yield at the CERN SPS. The Drell-Yan cross section is of interest here because it is the only source of lepton pairs in the mass region above the  $\psi'$  for  $\sqrt{S} = 17.3$  GeV. As such, it has been used to normalize the  $J/\psi$  yield and determine its suppression as a function of transverse energy,  $E_T$ . (See Ref. [13] for more details.) The NA50 collaboration [14] measures the dilepton continuum above 4 GeV in Pb+Pb collisions and fits the experimental  $K$  factor to the dilepton yield in the mass range  $4 < M < 9$  GeV by a LO Drell-Yan calculation with the MRSA [15] NLO PDFs. The Drell-Yan contribution below the  $J/\psi$  peak, in the range  $2.9 < M < 4.5$  GeV for NA50, is then calculated at LO and multiplied by this same experimental  $K$  factor, assuming that it is independent of mass and rapidity in the interval  $0 < y < 1$ . It is appropriate to check this assumption.

The Drell-Yan cross section as a function of mass and rapidity is also given by Eq. (13) with the delta function added for the mass, as explained earlier. We do not include any nuclear effects on the PDFs. The convolution of the prefactors  $H_{ii}^M$ , Eq. (15), with the

parton distribution functions in a nuclear collision in the  $q\bar{q}$  channel is:

$$\begin{aligned}
& \sum_{q_i \in Q} H_{ii}^M \left( f_{q_i}^N(x_1, Q^2) f_{\bar{q}_i}^N(x_2, Q^2) + f_{\bar{q}_i}^N(x_1, Q^2) f_{q_i}^N(x_2, Q^2) \right) \\
&= H_{uu}^M \left( \{Z_A f_u^p(x_1, Q^2) + N_A f_u^n(x_1, Q^2)\} \{Z_B f_{\bar{u}}^p(x_2, Q^2) + N_B f_{\bar{u}}^n(x_2, Q^2)\} \right. \\
&\quad \left. + 2AB f_c^p(x_1, Q^2) f_{\bar{c}}^p(x_2, Q^2) \right) \\
&\quad + H_{dd}^M \left( \{Z_A f_d^p(x_1, Q^2) + N_A f_d^n(x_1, Q^2)\} \{Z_B f_{\bar{d}}^p(x_2, Q^2) + N_B f_{\bar{d}}^n(x_2, Q^2)\} \right. \\
&\quad \left. + 2AB f_s^p(x_1, Q^2) f_{\bar{s}}^p(x_2, Q^2) \right) + [x_1 \leftrightarrow x_2, A \leftrightarrow B].
\end{aligned} \tag{23}$$

We let  $H_{uu}^M$  represent all charge  $+2/3$  quarks and  $H_{dd}^M$  all charge  $-1/3$  quarks. In the  $qg$  channel the convolution is

$$\begin{aligned}
& \sum_{q_i \in Q, \bar{Q}} H_{ii}^M \left( f_{q_i}^N(x_1, Q^2) f_g^N(x_2, Q^2) + f_g^N(x_1, Q^2) f_{q_i}^N(x_2, Q^2) \right) \\
&= B f_g^p(x_2, Q^2) \left\{ H_{uu}^M \left( \{Z_A f_u^p(x_1, Q^2) + N_A f_u^n(x_1, Q^2)\} \right. \right. \\
&\quad \left. \left. + \{Z_B f_{\bar{u}}^p(x_2, Q^2) + N_B f_{\bar{u}}^n(x_2, Q^2)\} + 2A f_c^p(x_1, Q^2) \right) \right. \\
&\quad \left. + H_{dd}^M \left( \{Z_A f_d^p(x_1, Q^2) + N_A f_d^n(x_1, Q^2)\} \right. \right. \\
&\quad \left. \left. + \{Z_B f_{\bar{d}}^p(x_2, Q^2) + N_B f_{\bar{d}}^n(x_2, Q^2)\} + 2A f_s^p(x_1, Q^2) \right) \right\} \\
&\quad + [x_1 \leftrightarrow x_2, A \leftrightarrow B].
\end{aligned} \tag{24}$$

We have taken the isospin of the nuclei into account, denoting the proton and neutron numbers in a nucleus with mass  $A$  by  $Z_A$  and  $N_A$  respectively.

Since we are interested in the makeup of the dilepton continuum in heavy ion collisions at the SPS, the values of  $\sqrt{S}$  and  $M$  relevant for our discussion are both considerably lower than in the previous section. We first present the Drell-Yan mass distributions in Fig. 3. At  $\sqrt{S} = 17.3$  GeV, the  $\gamma^* - Z$  and  $Z^0$  contributions to the Drell-Yan cross section, though included, are negligible. Note also that the slope of  $\sigma_{\text{LO}(1)}$  with  $M$  is different than  $\sigma_{\text{LO}(2)}$ . In particular,  $\sigma_{\text{LO}(1)}$  is similar to and larger than  $\sigma_{\text{LO}(2)}$  for  $M > 4$  GeV, where NA50 fits their data to the LO calculation, while, for  $M < m_{\psi'}$ ,  $\sigma_{\text{LO}(2)}$  is larger than  $\sigma_{\text{LO}(1)}$ . Thus, choosing a NLO PDF to fit an experimental  $K$  factor to a LO calculation could lead to some differences in the calculated Drell-Yan cross section below the  $J/\psi$  mass region.

The calculated  $K$  factors, shown in Fig. 4 as a function of  $M$ , demonstrate different dependencies on  $M$ . At this lower energy, all  $K$  factors are larger than for  $W^+$  production in the previous section. Some of this difference is because  $Q^2 = M^2 \ll m_W^2$  so that  $\alpha_s$  is larger for low mass Drell-Yan production. The standard  $K$  factor,  $K_{\text{th},0}^{(1)}$ , increases from  $\sim 1.75$  to 2.3 between 1 and 10 GeV while  $K_{\text{th},1}^{(1)}$  is nearly constant at  $\sim 1.95$  and  $K_{\text{th},2}^{(1)}$  decreases over the entire mass interval. None of these values agree with the constant experimental  $K$  factor of 1.7 [14] integrated over  $M$  obtained by NA50 with the MRSA [15] set. Since

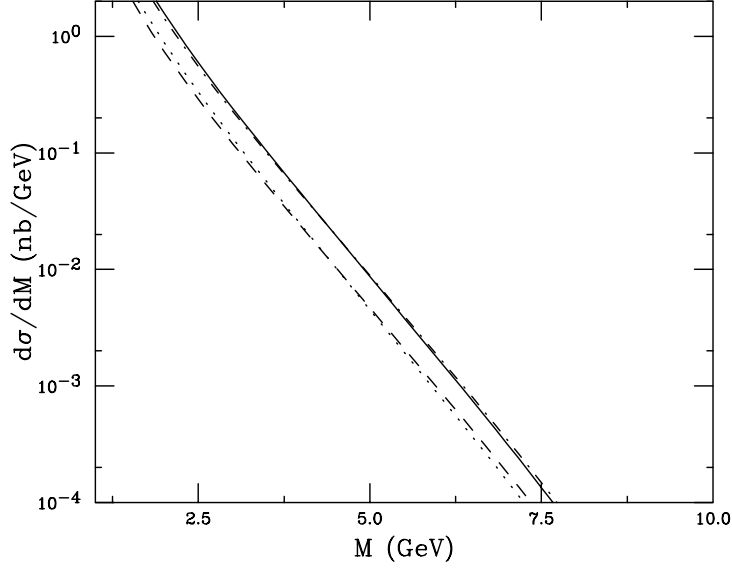


**Fig. 3.** The Drell-Yan mass distribution in Pb+Pb collisions at 17.3 GeV evaluated at  $Q = m$ . The solid curve is  $\sigma_{\text{NLO}(2)}$ , the dashed curve is  $\sigma_{\text{LO}(1)}$ , the dot-dashed curve is  $\sigma_{\text{NLO}(1)}$  and the dotted curve is  $\sigma_{\text{LO}(2)}$ .

the Drell-Yan data have relatively low statistics, a precise determination of the Drell-Yan cross section is difficult for  $M > 4$  GeV, especially when the Pb+Pb data are divided into centrality bins. Thus, any measure of changes in the slope of the mass distribution in Fig. 3 is unlikely in nuclear collisions at this energy. However, as shown in Figs. 3 and 4, the relative slopes and thus the theoretical  $K$  factors do change. A constant  $K$  factor cannot account for this. The ratios of the  $J/\psi$  to Drell-Yan cross sections used to represent the suppression pattern as a function of  $E_T$ , whether in the measured Drell-Yan or in the minimum bias analyses, both depend on extrapolation of  $\sigma_{\text{LO}(2)}$  multiplied by the experimental  $K$  factor.

The results for  $\sigma_{\text{LO}(2)}$  and  $\sigma_{\text{NLO}(2)}$  have also been calculated with the MRSA low  $Q^2$  PDF [15] used by NA50 [14]. Since there is no corresponding LO PDF for the MRSA set, we only compare  $K_{\text{th},0}^{(1)}$ . We find that  $\sigma_{\text{NLO}(2)}$  with MRSA is smaller than that with MRST for all masses, as much as 23% smaller at  $M = 10$  GeV. On the other hand,  $\sigma_{\text{LO}(2)}$  is a few percent larger with MRSA for  $M < 6$  GeV, dropping below the MRST cross section at higher masses by up to 16%. These differences are relatively small but, taken together, reduce  $K_{\text{th},0}^{(1)}$  for MRSA to  $\sim 1.8$  at 4 GeV, closer to the experimental  $K$  factor of NA50.

The Drell-Yan rapidity distributions and  $K$  factors are shown in Figs. 5 and 6 respectively. We have separated the results into three mass bins:  $2.9 < M < 4.5$ , the region in which NA50 compares the Drell-Yan and  $J/\psi$  data;  $4.5 < M < 6$  GeV; and  $6 < M < 9$

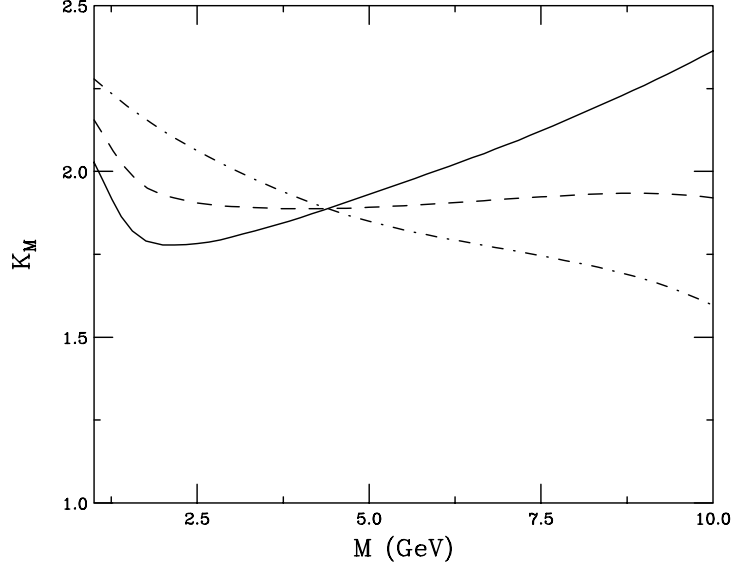


**Fig. 4.** The three  $K$  factors for Drell-Yan production at the SPS as a function of mass. The solid curve is  $K_{\text{th},0}^{(1)}$ , the dashed is  $K_{\text{th},1}^{(1)}$ , and the dot-dashed is  $K_{\text{th},2}^{(1)}$ .

GeV, above the  $J/\psi$  region. Of the latter two bins, the lower mass bin should correspond to the best statistics for NA50. Unfortunately, the NA50 Drell-Yan data are not binned in rapidity and are only given in the interval  $0 < y < 1$ . Note that the rapidity range becomes more restrictive as the mass increases. Only the lower two bins reach  $y = 1$ .

The trends of the cross sections as a function of mass in Fig. 3 are shown more clearly in Fig. 5. In the lower mass bin,  $\sigma_{\text{NLO}(2)} > \sigma_{\text{NLO}(1)}$  and  $\sigma_{\text{LO}(2)} > \sigma_{\text{LO}(1)}$  for  $y < 0.75$ . In the intermediate mass bin, the two ways of calculating the LO and NLO cross sections coincide up to  $y \approx 0.5$  where the results calculated with  $\sigma_{\text{LO}(1)}$  become larger. Finally, in the large mass bin,  $\sigma_{\text{NLO}(1)} > \sigma_{\text{NLO}(2)}$  and  $\sigma_{\text{LO}(1)} > \sigma_{\text{LO}(2)}$  for the entire rapidity range. The  $K$  factors as a function of rapidity reflect the cross section pattern. Again the  $K$  factors are all greater than 1.7 and, except for  $K_{\text{th},2}^{(1)}$ , are not constant but tend to grow with rapidity, especially  $K_{\text{th},0}^{(1)}$ .

Interestingly, when the cross sections are calculated with MRSA, the corresponding  $K_{\text{th},0}^{(1)}$  are always somewhat smaller than those with MRST and  $K_{\text{th},0}^{(1)} \sim 1.7$  near  $y \approx 0$  in the lowest mass bin. The agreement with NA50's experimental  $K$  factor is more likely a fortuitous accident than a precise fit. Given the rather limited Drell-Yan statistics of NA50 for  $M > 4$  GeV, it is doubtful that a better measure of the experimental  $K$  factor could have been obtained. It would be worthwhile, however, to calculate the full NLO cross section, either  $\sigma_{\text{NLO}(1)}$  or  $\sigma_{\text{NLO}(2)}$  depending on the chosen PDF, and obtain the experimental  $K$

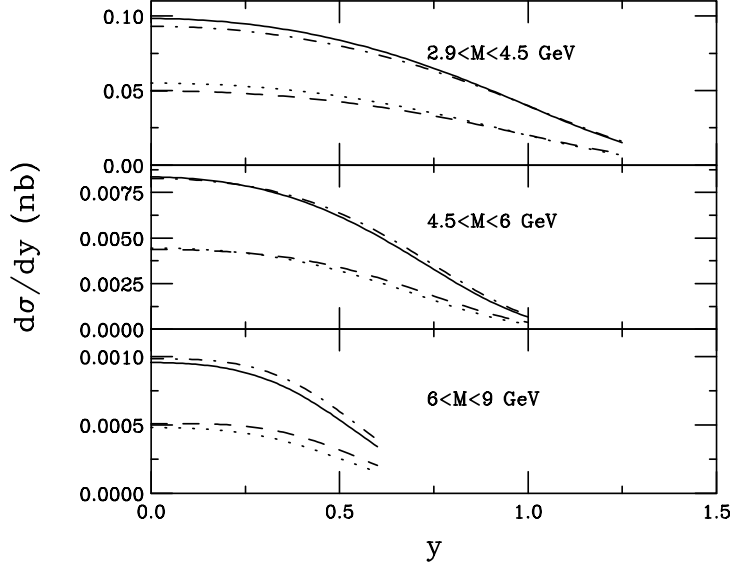


**Fig. 5.** The Drell-Yan rapidity distribution in Pb+Pb collisions at 17.3 GeV evaluated at  $Q = m$ . The solid curves are  $\sigma_{\text{NLO}(2)}$ , the dashed curves  $\sigma_{\text{LO}(1)}$ , the dot-dashed curves  $\sigma_{\text{NLO}(1)}$  and the dotted curves  $\sigma_{\text{LO}(2)}$ .

factor at NLO. Our results suggest that it would be significantly smaller but still above unity,  $\sim 1.2$ .

#### 4. Heavy Quark Production in $pp$ Interactions

We now turn to evaluations of the heavy quark cross sections and their  $K$  factors. We concentrate only on the bare distributions rather than introduce empirical fragmentation functions which, for heavy quarks, remain at a rather primitive level [16]. We can expect the biggest variations in the  $K$  factors here because the LO cross section is already proportional to  $\alpha_s^2$ . The order at which  $\alpha_s$  is calculated is important because the lower  $Q^2$ , proportional to  $m_T^2 = m_Q^2 + p_T^2$  in distributions, means  $\alpha_s$  is much larger for charm and bottom quarks than for gauge bosons. Differences in  $\Lambda_{\text{QCD}}$  between LO and NLO PDF fits result in similar values of  $\alpha_s$  at one and two loops when the LO and NLO values of  $\Lambda_{\text{QCD}}$  respectively are used. However, large discrepancies may result if the LO value of  $\Lambda_{\text{QCD}}$  is used in a two-loop evaluation of  $\alpha_s$ . Thus, one must be careful to use PDFs and  $\alpha_s$  evaluations that are compatible.

Heavy quarks are produced at LO by  $gg$  fusion and  $q\bar{q}$  annihilation while at NLO  $g(q + \bar{q})$  scattering is also included. To any order, the partonic cross section may be expressed in terms of dimensionless scaling functions  $f_{ij}^{(k,l)}$  that depend only on the variable  $\eta =$

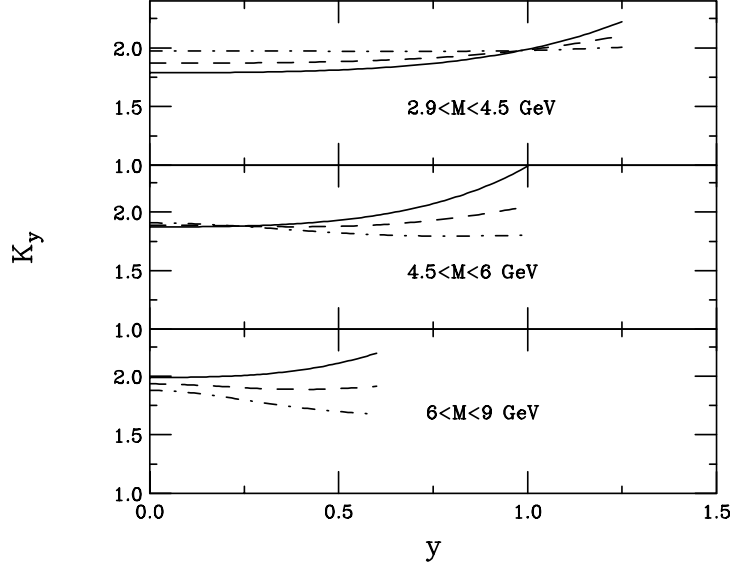


**Fig. 6.** The three  $K$  factors for Drell-Yan production at the SPS as a function of rapidity. The solid curves are  $K_{\text{th},0}^{(1)}$ , the dashed are  $K_{\text{th},1}^{(1)}$ , and the dot-dashed are  $K_{\text{th},2}^{(1)}$ .

$s/4m_Q^2 - 1$  [5],

$$\sigma_{ij}(s, m_Q^2, Q^2) = \frac{\alpha_s^2(Q^2)}{m_Q^2} \sum_{k=0}^{\infty} (4\pi\alpha_s(Q^2))^k \sum_{l=0}^k f_{ij}^{(k,l)}(\eta) \ln^l \left( \frac{Q^2}{m_Q^2} \right), \quad (25)$$

where  $s$  is the partonic center of mass energy squared,  $m_Q$  is the heavy quark mass and  $Q^2$  is the scale. The cross section is calculated as an expansion in powers of  $\alpha_s$  with  $k = 0$  corresponding to  $\sigma_{\text{LO}} = \sigma(\alpha_s^2)$ . The first correction,  $k = 1$ , corresponds to  $\sigma(\alpha_s^3)$ . Note that no distinction is made between LO and higher evaluations of  $\alpha_s$  in Eq. (25). The scale  $Q^2$  is generally assumed to be the same for both the renormalization,  $Q_R^2$ , and factorization,  $Q_F^2$ , scales since all PDF analyses make the assumption that  $Q_R^2 = Q_F^2 = Q^2$ . It is only when  $k \geq 1$  that the dependence on  $Q_R^2$  can be distinguished since when  $k = 1$  and  $l = 1$ , the logarithm  $\ln(Q^2/m_Q^2)$  appears. The dependence on  $Q_F^2$  appears already at LO in the argument of  $\alpha_s$  in the partonic cross section and in the parton densities. The NNLO corrections to next-to-next-to-leading logarithm with  $k = 2$  have been calculated near threshold [5]. The complete calculation only exists to NLO. The total hadronic cross section is obtained by convoluting the total partonic cross section with the PDFs,

$$\sigma_{pp}(S, m_Q^2) = \sum_{i,j=q,\bar{q},g} \int_{\frac{4m_Q^2}{S}}^1 d\tau \int_{\tau}^1 \frac{dx_1}{x_1} f_i^p(x_1, Q^2) f_j^p\left(\frac{\tau}{x_1}, Q^2\right) \sigma_{ij}(\tau S, m_Q^2, Q^2) \quad (26)$$

where the sums  $i$  and  $j$  are over all massless partons.

To illustrate the dependence of the total  $Q\bar{Q}$  cross sections upon  $m_Q$  and  $Q^2$ , we show the  $c\bar{c}$  and  $b\bar{b}$  cross sections as a function of mass and scale in Figs. 7 and 8. The charm

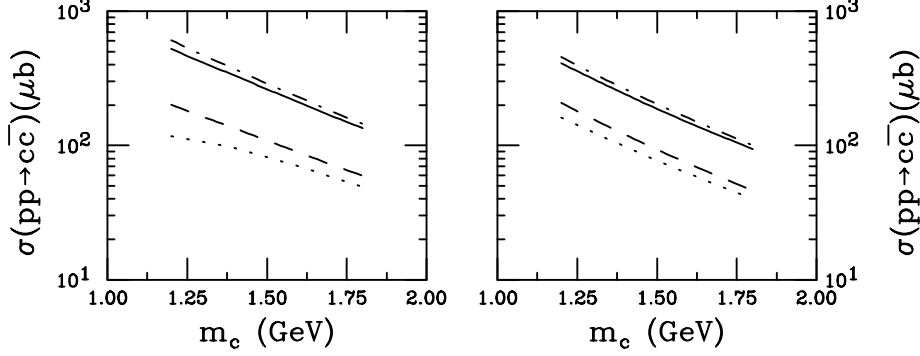


**Fig. 7.** The  $c\bar{c}$  total cross sections as a function of charm quark mass in  $pp$  collisions at 200 GeV. The lefthand plot shows the results for  $Q^2 = m_c^2$  while the righthand plot is calculated with  $Q^2 = 4m_c^2$ . The solid curves are  $\sigma_{\text{NLO}(2)}$ , the dashed curves  $\sigma_{\text{LO}(1)}$ , the dot-dashed curves  $\sigma_{\text{NLO}(1)}$  and the dotted curves  $\sigma_{\text{LO}(2)}$ .

mass is varied between 1.2 GeV and 1.8 GeV in  $\sqrt{s} = 200$  GeV  $pp$  collisions in Fig. 7. We choose this energy because it is close to that of the PHENIX charm measurement at RHIC [17],  $\sqrt{s} = 130$  GeV. A more complete measurement should be coming from the 200 GeV data taken in the latest run. The bottom mass is varied between 4.25 GeV and 5 GeV for  $pp$  collisions at  $\sqrt{s} = 41.6$  GeV, the energy of the HERA-B experiment which has recently presented a measurement of the  $b\bar{b}$  total cross section [18]. Unlike charm production at RHIC, bottom production at this energy is in the near-threshold region where resummation techniques can be applied [5].

The  $c\bar{c}$  cross section as a function of mass in Fig. 7 is calculated for two different values of the scale,  $Q^2 = m_c^2$  (left-hand side) and  $4m_c^2$  (right-hand side). Note that only scales greater than  $m_c^2$  are shown because  $Q^2 = m_c^2/4 < 1 \text{ GeV}^2$  for all charm masses considered, below the minimum scale of most PDFs. Thus results for scales lower than  $m_c^2$  would not be particularly meaningful. For this particular energy, the scale dependence is not strong, 10-20% at LO for  $m_c = 1.5$  GeV, and 40% at NLO. The stronger scale dependence at NLO is unusual and shows that charm could be difficult to treat at higher orders because of its relatively low mass [19]. The mass dependence is stronger for the NLO calculations than the LO and is also stronger for the larger scale. Note that in both cases displayed in Fig. 7  $\sigma_{\text{NLO}(2)} < \sigma_{\text{NLO}(1)}$  because  $\sigma_{\text{LO}(1)} > \sigma_{\text{LO}(2)}$ . The difference is small since  $K_{\text{th}}^{(1)} > 2$  for all three definitions of the  $K$  factor. Thus  $\sigma(\alpha_s^3)$  alone is significantly larger than either calculation of the LO cross section. The most important sources of the difference in the LO cross sections are the larger LO gluon density and the dominance of the  $gg$  production

channel. The charm  $K$  factors tend to be larger for lower masses and smaller scales.

We have shown the results for one specific energy here. However, the scale dependence changes with energy, as already noted in Section 2. The growth of the  $c\bar{c}$  total cross sections with energy is slower for  $Q^2 = m_c^2$ . At lower energies,  $\sigma(m_c^2) > \sigma(4m_c^2)$ . As the energy increases,  $\sigma(4m_c^2) > \sigma(m_c^2)$ . The value of  $\sqrt{S}$  at which this cross over occurs changes with  $m_c$ ,  $\sqrt{S} \approx 100$  GeV for  $m_c = 1.2$  GeV and  $\sqrt{S} \sim 3$  TeV for  $m_c = 1.8$  GeV. The change in energy dependence of the cross section with scale is due to the evolution of the PDFs at large  $Q^2$  and low  $x$ , similar to what was observed for  $W^+$  production in Section 2.

In Fig. 8, the  $b\bar{b}$  cross section is given as a function of mass for three different values of  $Q^2$ ,  $m_b^2/4$  (upper left),  $m_b^2$  (upper right) and  $4m_b^2$  (bottom center). The larger bottom quark

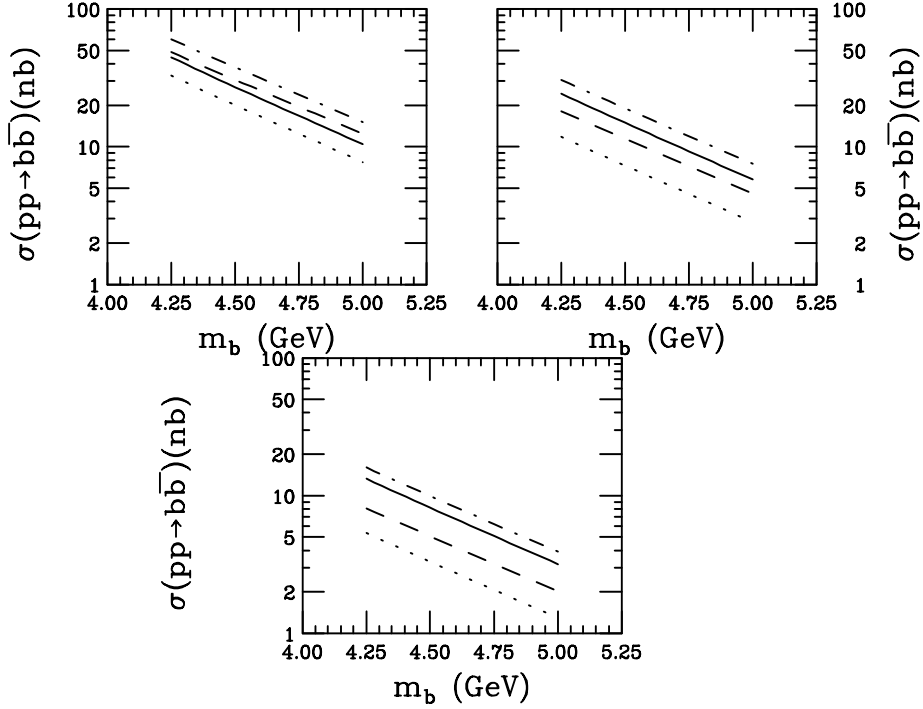


**Fig. 8.** The  $b\bar{b}$  total cross sections as a function of bottom quark mass in  $pp$  collisions at 41.6 GeV. Clockwise from the upper left, the results are calculated with  $Q^2 = m_b^2/4$ ,  $m_b^2$ , and  $4m_b^2$  respectively. The solid curves are  $\sigma_{\text{NLO}(2)}$ , the dashed curves  $\sigma_{\text{LO}(1)}$ , the dot-dashed curves  $\sigma_{\text{NLO}(1)}$  and the dotted curves  $\sigma_{\text{LO}(2)}$ .

mass now allows us to calculate the cross section for scales lower than  $m_b^2$  and still obtain meaningful results. In this case, the scale dependence is reduced at NLO relative to LO. The mass dependence is stronger at NLO, as for charm, and increases somewhat with scale. The heavier quark mass reduces the impact of  $\sigma(\alpha_s^3)$  on the total cross sections. Indeed,



for  $Q^2 = m_b^2/4$ ,  $\sigma_{\text{LO}(1)} > \sigma_{\text{NLO}(2)}$ . This effect is probably due to the one-loop  $\alpha_s$  evaluation in  $\sigma_{\text{LO}(1)}$  since the one-loop  $\alpha_s$  is larger than the two-loop  $\alpha_s$ , particularly at low scales. The bottom  $K$  factors are all smaller than those for charm,  $K_{\text{th}}^{(1)} < 2$  in most cases. Thus  $b\bar{b}$  production, at least at this energy, is better under control than charm. Like charm, however, the  $K$  factors also are larger for lower masses and higher scales. The scale dependence of  $b\bar{b}$  production with energy is smaller than for charm. The bottom cross sections follow the hierarchy  $\sigma(m_b^2/4) > \sigma(m_b^2) > \sigma(4m_b^2)$  for all energies and orders. Near threshold the difference in cross sections due to scale can be nearly a factor of 10 but by  $\sqrt{s} = 14$  TeV, the difference is only a few percent. The smaller scale dependence is also an indication that bottom production is better under control than charm.

The mass and scale parameters used in our further calculations are determined by obtaining a ‘best’ fit to the data without an experimental  $K$  factor. Using the MRST PDFs to calculate  $\sigma_{\text{NLO}(2)}$ , we found  $m_c = 1.2$  GeV and  $Q^2 = 4m_c^2$  and  $m_b = 4.75$  GeV with  $Q^2 = m_b^2$  for bottom [20–22]. Although there is a great deal of scattered data up to  $\sqrt{s} = 63$  GeV on the  $c\bar{c}$  total cross section, our choice for the bottom parameters are in line with conventional wisdom rather than data. When other PDFs were used, the parameters favored varied somewhat [21, 22] but, in the following, we compare results from different PDFs using the same values of  $m_Q$  and  $Q^2$ .

Since the charm mass obtained from these evaluations is somewhat smaller than the 1.5 GeV mass generally used and the NLO calculations with  $m_b = 4.75$  GeV underestimate the Tevatron  $p\bar{p} \rightarrow b\bar{b}$  data [23], it is reasonable to expect that higher order corrections beyond NLO could be large. Indeed, the HERA-B cross section [18] agrees with the NNLO-NNLL cross section in Ref. [5], suggesting that the next order correction could be nearly a factor of two. Thus the NNLO correction could be nearly as large as the total NLO cross section.

Unfortunately, the NNLO-NNLL calculation is valid only near threshold. The  $p\bar{p}$  data at higher energies, while not total cross sections, also show a large discrepancy between the perturbative NLO result and the data, nearly a factor of three [23]. This difference could be accounted for using unintegrated parton densities [24] although these unintegrated distributions vary widely. Another, more mundane explanation to the  $b\bar{b}$  discrepancy is an incomplete understanding of the hadronization process [3]. If some resummation is needed in the high energy regime to account for the Tevatron data, there remains the difficulty of connecting the regimes where near-threshold corrections are applicable and where high-energy, small  $x \sim m_Q/\sqrt{s}$  physics dominates. This problem is increased for charm where, even at low energies, we are far away from threshold.

Our method is perhaps the most straightforward—using  $\sigma_{\text{NLO}(2)}$  and ignoring higher-order corrections to fit the data. This is not difficult for  $c\bar{c}$  because the data are extensive. However, there are less  $b\bar{b}$  data. The  $\pi^- p \rightarrow c\bar{c}$  data tend to favor lighter charm masses. It is difficult to say if the same is true for  $b\bar{b}$ . A value of  $m_b = 4.75$  GeV, which underpredicts the Tevatron results compared to NLO cross sections [23], agrees reasonably well with the average of the  $\pi^- p$  data. However, for the HERA-B measurement to be compatible with a NLO evaluation, the  $b$  quark mass would have to be reduced to 4.25 GeV, a value which might be more compatible with the Tevatron results. Therefore, a full NNLO calculation with  $m_c \sim 1.5$  GeV and  $m_b \sim 4.75$  GeV might agree with the  $Q\bar{Q}$  data without

an experimental  $K$  factor. A more quantitative statement is not possible.

We now employ our inferred values of  $m_Q$  and  $Q^2$  to calculate the  $K$  factors as functions of energy and PDF. Figure 9 illustrates the danger inherent in calculating,  $\sigma_{\text{LO}(1)}$  and then multiplying either by  $K_{\text{th},0}^{(1)}$  or by an arbitrary factor of 2: the cross sections can be considerably overestimated. Indeed,  $K$  factors are generally applied to avoid underestimating

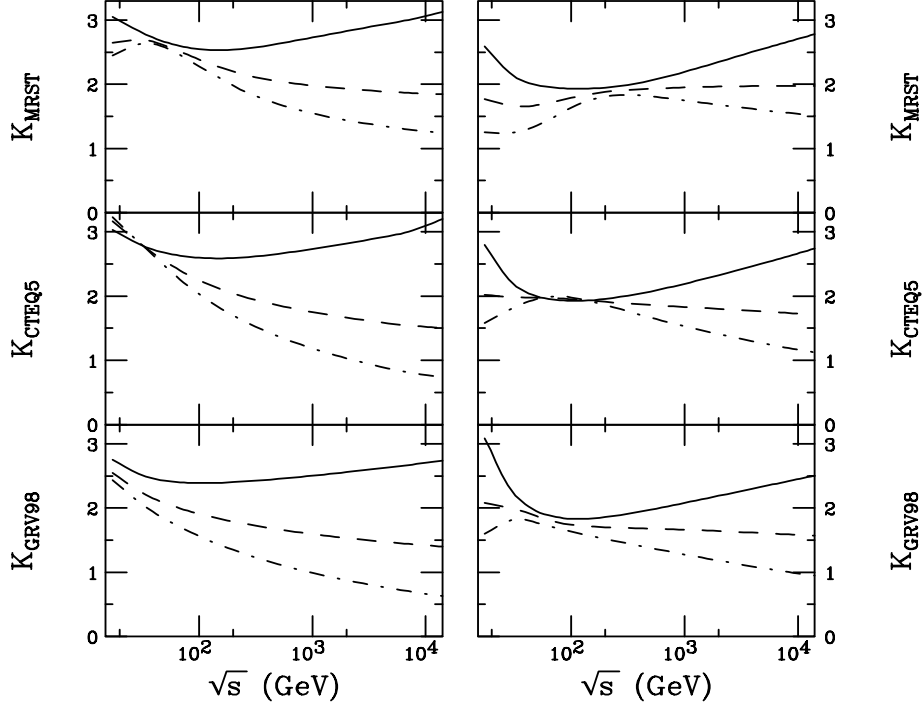


**Fig. 9.** The three  $K$  factors for  $Q\bar{Q}$  production in  $pp$  collisions as a function of energy. The  $c\bar{c}$  results, calculated with  $m_c = 1.2$  GeV and  $Q^2 = 4m_c^2$ , are given on the lefthand side, while the  $b\bar{b}$ , calculated with  $Q^2 = m_b^2$  and  $m_b = 4.75$  GeV, are on the righthand side. From top to bottom the results are given for the MRST, CTEQ5, and GRV 98 PDFs. The solid curves are  $K_{\text{th},0}^{(1)}$ , the dashed are  $K_{\text{th},1}^{(1)}$ , and the dot-dashed are  $K_{\text{th},2}^{(1)}$ .

the cross sections. We see that  $K_{\text{th},0}^{(1)}$  is generally greater than 2 at low energies, drops somewhat and finally increases with energy. This dependence of the standard  $K$  factor could be attributed to more inherent theoretical uncertainties in low and high energies where different resummation techniques are applicable. There is a somewhat stronger effect for  $b\bar{b}$  since  $2m_b/\sqrt{s} \geq 0.1$ , near the threshold region, until  $\sqrt{s} \sim 100$  GeV. On the other hand, charm production is well above threshold for all energies shown since  $2m_c/\sqrt{s} \leq 0.1$  for  $\sqrt{s} > 20$  GeV. Note that  $K_{\text{th},1}^{(1)}$  and  $K_{\text{th},2}^{(1)}$  both decrease with energy with a larger decrease

for  $c\bar{c}$  (lefthand plots) than  $b\bar{b}$  (righthand plots). This decrease can clearly be attributed to decreasing  $x \sim \sqrt{Q^2/S}$  with increasing  $\sqrt{S}$ . The  $x$  range of charm production is from  $x \sim 0.1$  at 15 GeV to  $10^{-4}$  at 14 TeV. The LO gluon PDF is larger than the NLO gluon PDF, particularly at low scales, so that  $\sigma_{\text{LO}(1)}$  increases faster than  $\sigma_{\text{NLO}(2)}$  and  $K_{\text{th},2}^{(1)}$  decreases to near or below unity at high energies. The values of  $x$  and  $Q^2$  are larger for  $b\bar{b}$  production so that the decrease in  $K_{\text{th},2}^{(1)}$  with energy is slower.  $K_{\text{th},1}^{(1)}$  does not decrease as quickly as  $K_{\text{th},2}^{(1)}$ , and is almost independent at high energies, but is still smaller than  $K_{\text{th},0}^{(1)}$ . Thus at high energies,  $\sigma_{\text{LO}(1)} \sim \sigma_{\text{NLO}(2)}$  in some cases and including a  $K$  factor on  $\sigma_{\text{LO}(1)}$  would overestimate the cross section by a factor of 2 – 3. The same trends are observed for results with the CTEQ5 and GRV 98 PDFs.

The PDF dependence is illustrated in Fig. 10 with the ratios of the CTEQ5 and GRV 98 LO and NLO cross sections to the MRST cross sections. The ratios depend most strongly

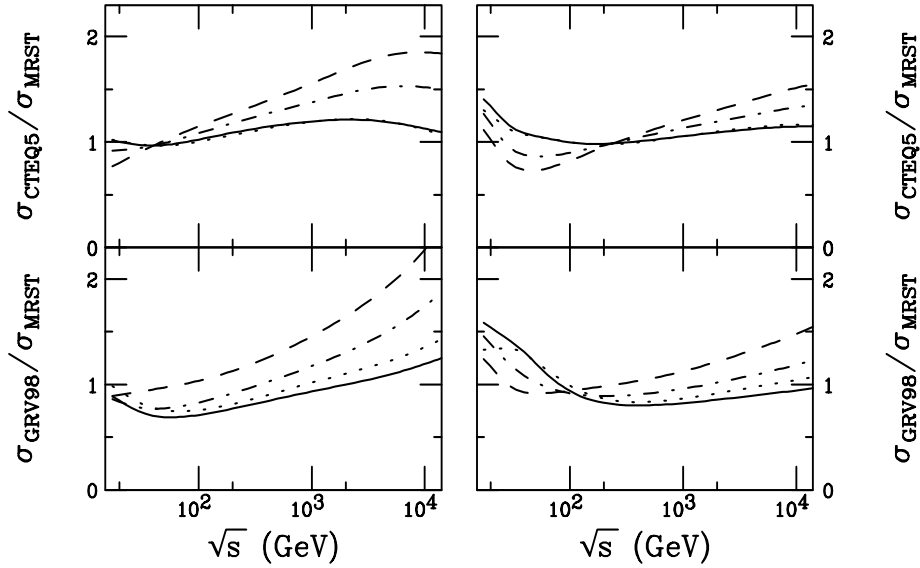


**Fig. 10.** Ratios of the total  $Q\bar{Q}$  cross sections calculated with the CTEQ5 (top) and GRV 98 (bottom) PDFs to those calculated with the MRST PDFs as a function of energy. The  $c\bar{c}$  results, calculated with  $m_c = 1.2$  GeV and  $Q^2 = 4m_c^2$ , are given on the lefthand side, while the  $b\bar{b}$ , calculated with  $Q^2 = m_b^2$  and  $m_b = 4.75$  GeV, are on the righthand side. The solid ratios are  $\sigma_{\text{NLO}(2)}$ , the dashed ratios  $\sigma_{\text{LO}(1)}$ , the dot-dashed ratios  $\sigma_{\text{NLO}(1)}$  and the dotted ratios  $\sigma_{\text{LO}(2)}$ .

on the relative gluon PDFs. The CTEQ5 and MRST NLO gluon distributions are very similar so that the ratios of  $\sigma_{\text{LO}(2)}$  and  $\sigma_{\text{NLO}(2)}$  are nearly unity without much variation over the entire energy range. There are slight differences for  $b\bar{b}$  at low energies due to the

larger  $q\bar{q}$  contribution near threshold. The GRV 98 NLO gluon distribution is less similar to the MRST gluon, leading to a larger variation of the ratios with energy. The ratios involving the LO gluon PDFs are larger and more energy dependent because the LO gluon distribution is not as well constrained. The biggest differences are in the ratios of  $\sigma_{\text{LO}(1)}$  since the large  $gg$  contribution to  $\sigma(\alpha_s^3)$  reduces the effect of the LO gluon distribution in the  $\sigma_{\text{NLO}(1)}$  ratios.

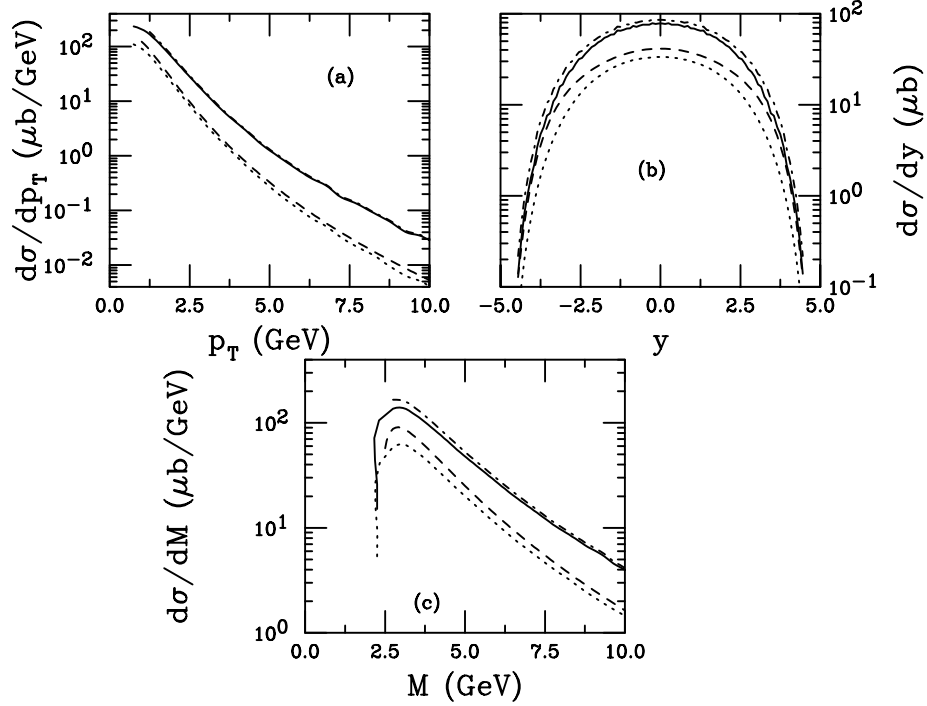


**Fig. 11.** The charm quark  $p_T$  (a), rapidity (b), and  $c\bar{c}$  pair mass (c) for  $pp$  collisions at 200 GeV. The solid curve is  $\sigma_{\text{NLO}(2)}$ , the dashed curve is  $\sigma_{\text{LO}(1)}$ , the dot-dashed curve is  $\sigma_{\text{NLO}(1)}$  and the dotted curve is  $\sigma_{\text{LO}(2)}$ .

To complete our discussion of heavy quarks, we now turn to the charm and bottom distributions and their corresponding  $K$  factors, shown in Figs. 11-14. The necessity of NLO evaluations of  $Q\bar{Q}$  production is clear if one wants to study pair production and correlations. The  $p_T$  of the  $Q\bar{Q}$  pair is zero at LO and only becomes finite at NLO. LO calculations are thus only useful for obtaining the single quark distributions in  $p_T$ , rapidity and Feynman  $x$ ,  $x_F$ , and for the  $Q\bar{Q}$  pair, the  $y$ ,  $x_F$  and invariant mass,  $M$ , distributions. Therefore the quantities for which we calculate the  $K$  factor, besides the total cross sections, are the single quark  $p_T$  and rapidity distributions and the pair mass distribution. We will evaluate the differential  $K$  factors for charm distributions at RHIC,  $\sqrt{s} = 200$  GeV, and bottom at

the LHC,  $\sqrt{S} = 5.5$  TeV, both appropriate energies for ion colliders. We calculate  $\sigma_{\text{LO}(1)}$

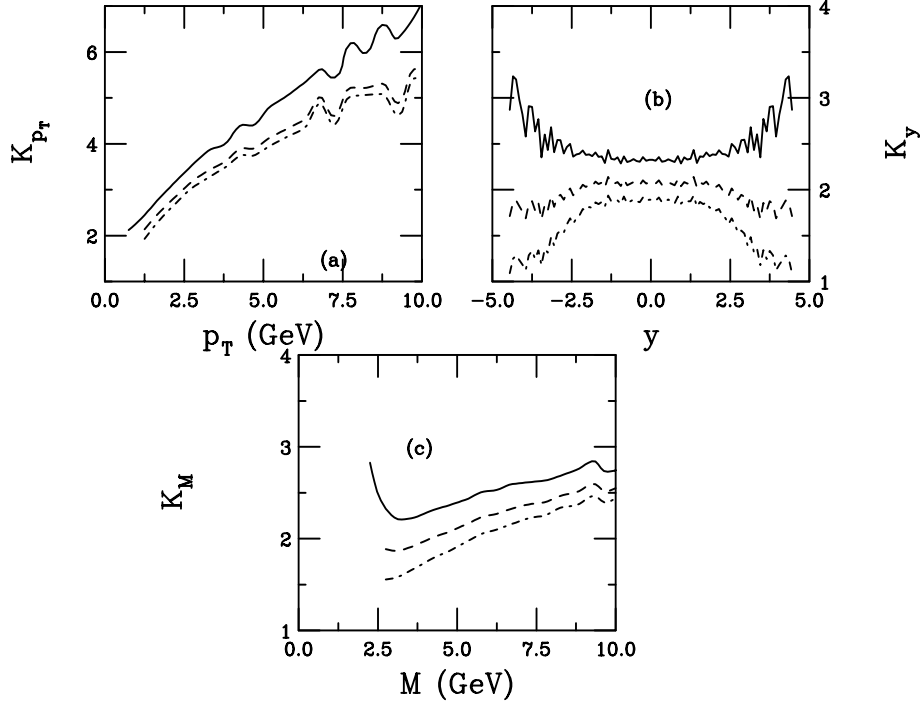


**Fig. 12.** The three  $K$  factors as a function of charm quark  $p_T$  (a), rapidity (b), and  $c\bar{c}$  pair mass (c) for  $pp$  collisions at 200 GeV. The solid curve is  $K_{\text{th},0}^{(1)}$ , the dashed is  $K_{\text{th},1}^{(1)}$ , and the dot-dashed is  $K_{\text{th},2}^{(1)}$ .

analytically, resulting in smooth distributions. However,  $\sigma_{\text{LO}(2)}$  and  $\sigma(\alpha_s^3)$  are calculated with the NLO Monte Carlo code described in Ref. [25] which uses a two-loop evaluation of  $\alpha_s$  as a default. The finite statistics of the Monte Carlo result in some fluctuations in the distributions, particularly apparent in the  $K$  factors.

The charm calculations at  $\sqrt{S} = 200$  GeV for RHIC correspond to the total cross sections shown in Fig. 7 with  $m_c = 1.2$  GeV and  $Q^2 = 4m_c^2$ . It is clear that the LO  $p_T$  distributions in Fig. 11 have a steeper slope than the NLO distributions. The charm rapidity and pair mass distributions, on the other hand, are more similar. The  $K$  factors increase rapidly with  $p_T$  in Fig. 12 even though we have used  $m_T^2$  as a more appropriate scale for the distributions [26]. This increase can be expected since  $\sigma(\alpha_s^3)$  is inherently at higher  $p_T$  due to contributions from  $gg \rightarrow gg^* \rightarrow gQ\bar{Q}$  where the  $Q\bar{Q}$  pair is opposite a gluon jet. Contributions such as these begin to be important when  $p_T > m_Q$ , as is obvious in Fig. 12. The increase in the  $K$  factor with  $p_T$  is also only important when  $x$  is relatively small—the

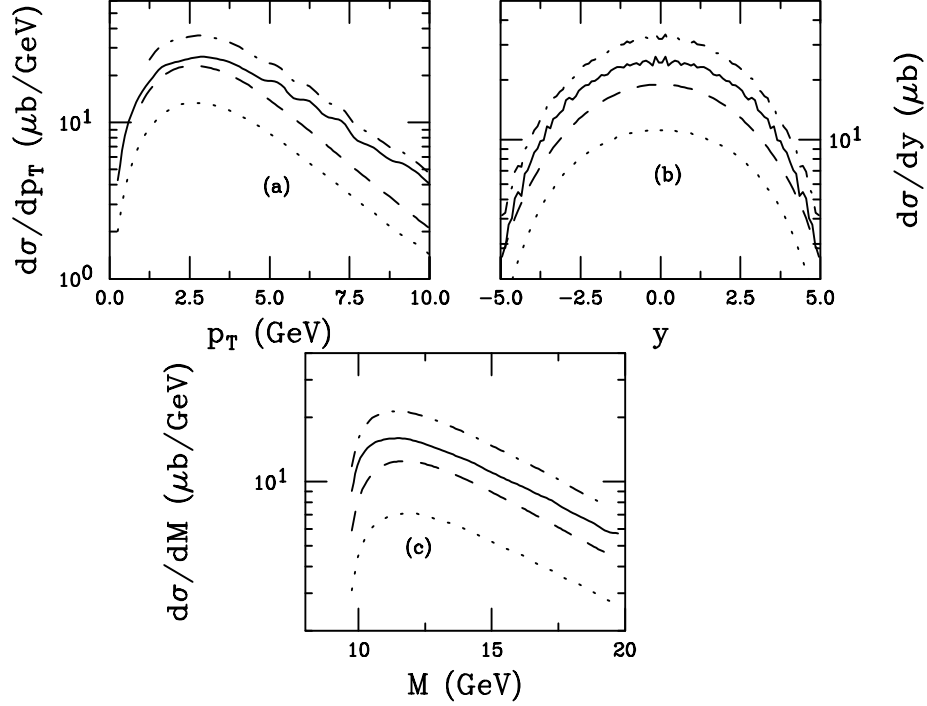


**Fig. 13.** The bottom quark  $p_T$  (a), rapidity (b), and  $b\bar{b}$  pair mass (c) for  $pp$  collisions at 5.5 TeV. The solid curve is  $\sigma_{\text{NLO}(2)}$ , the dashed curve is  $\sigma_{\text{LO}(1)}$ , the dot-dashed curve is  $\sigma_{\text{NLO}(1)}$  and the dotted curve is  $\sigma_{\text{LO}(2)}$ .

$K$  factors for  $b\bar{b}$  production at RHIC increase very slowly with  $p_T$  over the same interval. The  $p_T$  dependence of the  $K$  factors clearly should be taken into account when scaling up a LO calculation. Conversely, the  $K$  factors are nearly constant with rapidity and pair mass which are  $p_T$ -integrated and are weighted by the low  $p_T$  part of the cross section. The same trend with rapidity seen in Figs. 2 and 6 is also observed here:  $K_{\text{th},0}^{(1)}$  increases slowly with rapidity while  $K_{\text{th},2}^{(1)}$  decreases. The exact behavior at large rapidity is difficult to determine because the Monte Carlo fluctuations are largest near the edges of phase space.

A careful examination of the  $K$  factors may reveal some slight difference in magnitude between Figs. 12 and 9 at the same energy. This shift is due to the somewhat different scales used to calculate total cross sections and distributions. For total cross sections, the only relevant scale is  $Q^2 \propto m_Q^2$  in the  $\ln(Q^2/m_Q^2)$  term in Eq. (25). However, when calculating distributions,  $p_T$ -dependent logarithms also enter which need to be controlled by the  $m_T$  scale. Shifting the scale from  $\propto m_Q^2$  to  $\propto m_T^2$  has the effect of modifying the total cross section obtained by integrating the distributions. This shift in scale is manifested by a

change in the magnitude of the  $K$  factors as well.

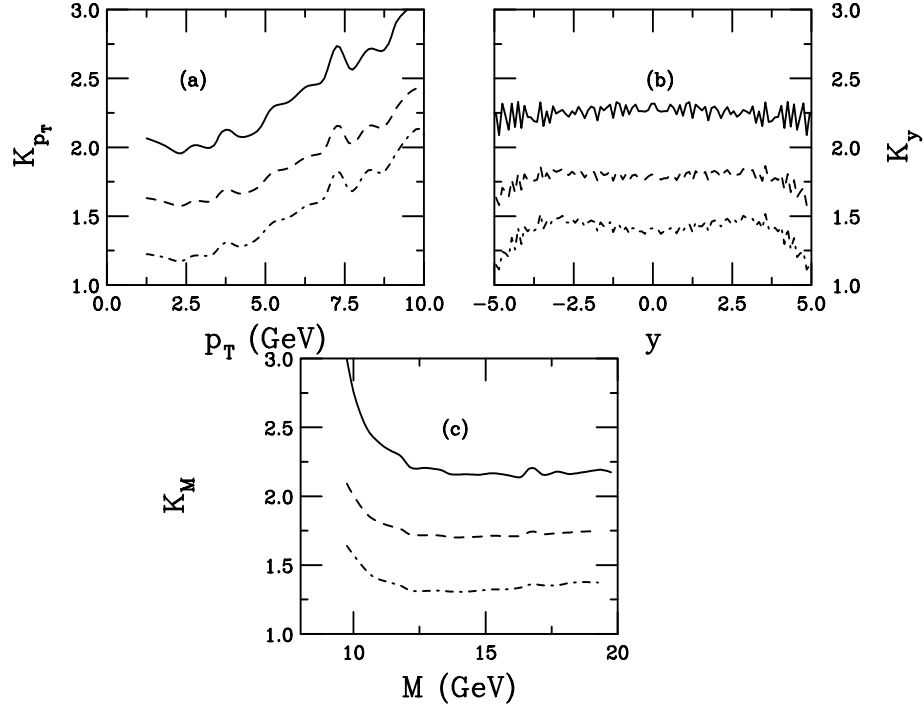


**Fig. 14.** The three  $K$  factors as a function of bottom quark  $p_T$  (a), rapidity (b), and  $b\bar{b}$  pair mass (c) for  $pp$  collisions at 5.5 TeV. The solid curve is  $K_{th,0}^{(1)}$ , the dashed is  $K_{th,1}^{(1)}$ , and the dot-dashed is  $K_{th,2}^{(1)}$ .

The results for  $b\bar{b}$  production in  $\sqrt{S} = 5.5$  TeV  $pp$  collisions at the LHC are shown in Figs. 13 and 14. The  $K$  factors clearly begin to increase for  $p_T > 5$  GeV where  $p_T > m_b$ . The increase with  $p_T$  is slower than for charm production. The  $K$  factors are essentially constant over the rapidity range shown since the edge of phase space has not yet been reached at  $y = 5$ . Also, away from threshold,  $2m_b$ , the  $K$  factors are constant as a function of mass. Note that  $K_{th,0}^{(1)}$  exhibits the strongest threshold effect near  $M \sim 10$  GeV.

## 5. Summary

We have discussed three ways of defining the theoretical  $K$  factor to NLO. The first,  $K_{th,0}^{(1)}$ , is most appropriate for determining the theoretical uncertainties between cross sections of different orders because it allows the most straightforward determination of the next-order

effects. In cases where the use of the LO cross section is necessary for speed of calculation, such as in event generators, it is most appropriate to make a full LO evaluation and then multiply by either  $K_{\text{th},1}^{(1)}$  or  $K_{\text{th},2}^{(1)}$ .

We have shown that the theoretical  $K$  factor is only approximately constant away from threshold and away from the edges of phase space. Thus for high energy  $W^+$  production,  $K$  is only independent of rapidity for  $y < 2$ . The Drell-Yan  $K$  factor is not constant with mass, increasing at low masses and also changing at high masses, increasing or decreasing depending on which definition is used. The rapidity range over which  $K$  is constant for Drell-Yan production at the SPS decreases with increasing mass as the edge of phase space is approached at lower rapidities. The  $K$  factors for heavy quarks are most strongly dependent on  $p_T$  since the NLO corrections are large for  $p_T \geq m_Q$ . Similarly, a strong dependence of  $K_{\text{th},0}^{(1)}$  on  $p_T$  in inclusive jet production was found in Ref. [6].

Clearly a constant  $K$  factor is inappropriate for all kinematic variables. To best utilize knowledge of the next-to-leading and higher order corrections, the differential  $K$  factor should be determined as a function of the kinematic variables of interest, such as  $p_T$ ,  $y$  or  $M$ . Whether  $K_{\text{th},1}^{(1)}$  or  $K_{\text{th},2}^{(1)}$  is used with  $\sigma_{\text{LO}(1)}$  is somewhat a matter of taste. However, it should perhaps be kept in mind that the PDFs are evaluated to NLO using  $\sigma_{\text{NLO}(2)}$ . Thus  $K_{\text{th},2}^{(1)}$  is perhaps the most relevant for extending full LO calculations to NLO. Therefore there is no clearcut answer to the question posed in the title. Whatever definition is chosen, it is obviously important that the determination of  $K_{\text{th}}$  be clearly described and applied consistently in a given calculation.

**Acknowledgements** I thank G. Fai, P. Levai, and I. Vitev for encouragement and helpful discussions.

## References

1. M. Kramer, *Prog. Part. Nucl. Phys.* **47** (2001) 141.
2. T. Sjöstrand, *Comput. Phys. Commun.* **82** (1994) 74. Program updates and documentation can be found at <http://www.thep.lu.se/tf2/staff/torbjorn/Pythia.html>.
3. M. Cacciari and P. Nason, hep-ph/0204025.
4. R. Hamberg, W.L. van Neerven and T. Matsuura, *Nucl. Phys.* **B359** (1991) 343.
5. N. Kidonakis, E. Laenen, S. Moch, and R. Vogt, *Phys. Rev.* **D64** (2001) 114001.
6. G.G. Barnafoldi, G. Fai, P. Lévai, G. Papp and Y. Zhang, *J. Phys.* **G27** (2001) 1767.
7. A.D. Martin, R.G. Roberts, and W.J. Stirling, and R.S. Thorne, *Eur. Phys. J.* **C4** (1998) 463.
8. A.D. Martin, R.G. Roberts, and W.J. Stirling, and R.S. Thorne, *Phys. Lett.* **B443** (1998) 301.
9. R. Vogt, *Phys. Rev.* **C64** (2001) 044901.
10. B.W. Harris, J. Smith, and R. Vogt, *Nucl. Phys.* **B461** (1996) 181.
11. H.L. Lai *et al.*, *Eur. Phys. J.* **C12** (2000) 375.
12. M. Glück, E. Reya, and A. Vogt, *Eur. Phys. J.* **C5** (1998) 461.
13. R. Vogt, *Phys. Rept.* **310** (1999) 197.
14. M.C. Abreu *et al.* (NA50 Collab.), *Phys. Lett.* **B410** (1997) 327, 337.



15. A.D. Martin, R.G. Roberts and W.J. Stirling, *Phys. Rev.* **D51** (1995) 4756.
16. C. Peterson, D. Schlatter, I. Schmitt, and P. Zerwas, *Phys. Rev.* **D27** (1983) 105.
17. K. Adcox *et al.* (PHENIX Collab.), *Phys. Rev. Lett.* **88** (2002) 192303.
18. I. Abt *et al.* (HERA-B Collab.), hep-ex/0205106.
19. J. Smith and R. Vogt, *Z. Phys.* **75** (1997) 271.
20. R. Vogt, to appear in the Proceedings of the Hard Probe Collaboration, LBNL-45350, hep-ph/0111271.
21. R. Vogt, in proceedings of the '18<sup>th</sup> Winter Workshop on Nuclear Dynamics', Nassau, The Bahamas, edited by W. Bauer *et al.*, hep-ph/0203152.
22. R. Vogt, in proceedings of the 'Budapest'02 Workshop on Quark and Hadron Dynamics', Budapest, Hungary, edited by P. Lévai *et al.*, hep-ph/0205330.
23. T. Affolder *et al.* (CDF Collab.), *Phys. Rev. Lett.* **84** (2000) 232.
24. A.P. Lipatov, V.A. Saleev and N.P. Zotov, hep-ph/0112114.
25. M.L. Mangano, P. Nason and G. Ridolfi, *Nucl. Phys.* **B405** (1993) 507.
26. R. Vogt, *Z. Phys.* **C71** (1996) 475.